nanomaterials

MDPI

Article

TiO_2 Nanotube Layers Decorated with $Al_2O_3/MoS_2/Al_2O_3$ as Anode for Li-ion Microbatteries with Enhanced Cycling Stability

Alexander Teklit Tesfaye [1], Hanna Sopha [2,3], Angela Ayobi [1], Raul Zazpe [2,3], Jhonatan Rodriguez-Pereira [2], Jan Michalicka [3], Ludek Hromadko [2,3], Siowwoon Ng [3], Zdenek Spotz [3], Jan Prikryl [2], Jan M. Macak [2,3] and Thierry Djenizian [1,4,*]

1 Mines Saint-Etienne, Center of Microelectronics in Provence, Flexible Electronics Department, 13541 Gardanne, France; alexanderteklit@gmail.com (A.T.T.); angieayobi@gmail.com (A.A.)
2 Center of Materials and Nanotechnologies, Faculty of Chemical Technology, University of Pardubice, Nam. Cs. Legii 565, 53002 Pardubice, Czech Republic; HannaIngrid.Sopha@upce.cz (H.S.); Raul.Zazpe@upce.cz (R.Z.); Jhonatan.RodriguezPereira@upce.cz (J.R.-P.); Ludek.Hromadko@upce.cz (L.H.); Jan.Prikryl@upce.cz (J.P.); Jan.Macak@upce.cz (J.M.M.)
3 Central European Institute of Technology, Brno University of Technology, Purkyňova 123, 612 00 Brno, Czech Republic; jan.michalicka@ceitec.vutbr.cz (J.M.); SiowWoon.Ng@ceitec.vutbr.cz (S.N.); Zdenek.Spotz@ceitec.vutbr.cz (Z.S.)
4 Al-Farabi Kazakh National University, Center of Physical-Chemical Methods of Research and Analysis, 96A. Tole bi str., 050012 Almaty, Kazakhstan
* Correspondence: thierry.djenizian@emse.fr

Received: 16 April 2020; Accepted: 12 May 2020; Published: 17 May 2020

Abstract: TiO_2 nanotube layers (TNTs) decorated with $Al_2O_3/MoS_2/Al_2O_3$ are investigated as a negative electrode for 3D Li-ion microbatteries. Homogenous nanosheets decoration of MoS_2, sandwiched between Al_2O_3 coatings within self-supporting TNTs was carried out using atomic layer deposition (ALD) process. The structure, morphology, and electrochemical performance of the $Al_2O_3/MoS_2/Al_2O_3$-decorated TNTs were studied using scanning transmission electron microscopy, energy dispersive X-ray spectroscopy, X-ray photoelectron spectroscopy, and chronopotentiometry. $Al_2O_3/MoS_2/Al_2O_3$-decorated TNTs deliver an areal capacity almost three times higher than that obtained for MoS_2-decorated TNTs and as-prepared TNTs after 100 cycles at 1C. Moreover, stable and high discharge capacity (414 μAh cm^{-2}) has been obtained after 200 cycles even at very fast kinetics (3C).

Keywords: TiO_2 nanotube; MoS_2; Al_2O_3; atomic layer deposition; Li-ion microbatteries

1. Introduction

Nowadays, microelectrochemical systems are key devices for providing power for micro/nanoelectromechanical devices (M/NEMS) in the fields of bio/medical engineering, aerospace, and intelligent sensors [1–3]. The microelectrochemical systems can be classified based on their power source as rechargeable Li-ion microbatteries (μLIBs) [4–6], microsupercapacitors [7], microfuel cells [8], and microthermoelectric batteries [9]. The two main requirements for selecting power sources for M/NEMS devices are high energy/power densities and long lifetime [10,11]. Planar 2D μLIBs energy and power densities have an intrinsically inverse correlation, i.e., microbatteries with thick electrodes deliver a high-energy and a low-power density, while the reverse is true for thin electrodes [12]. Hence, the development of 3D μLIBs forms a viable alternative to planar 2D μLIBs to overcome the tradeoff between power and energy [13,14]. Nanomaterials such as nanopillars, nanorods, nanowires,

and nanotubes are widely explored as potential electrode materials for 3D μLIBs due to their short ion diffusion distances, high aspect ratio, and small foot print [15–18].

Self-supported TiO_2 nanotube (TNT) layers have been extensively explored as anodes for 2D/3D μLIBs due to their unique one-dimensional architecture, high self-ordering degree, short Li^+ diffusion distance, fast electron transport, safety (high lithiation potential ~1.7 V vs. Li/Li^+), low self-discharge rate, and nontoxic nature [18–22]. However, their low theoretical capacity (168 mAh g^{-1}) and poor electronic conductivity pose a major obstacle for practical application [20,23,24].

To overcome these problems, surface modification of the TNT layers by coating, decorating, and doping with various materials have been extensively explored [6,25–38]. Because of the low volumetric expansion and high porosity, the surface modified TNT layers deliver high capacity, while keeping the mechanical stability of the nanostructured electrode. In our recent work, we showed, for the first time, TNT layers homogenously decorated with ultrathin MoS_2 nanosheets using atomic layer deposition (ALD) process that can be used as anode for 3D μLIBs [6]. The MoS_2-decorated TNT layers deliver superior electrochemical performance in comparison to their pristine counterparts. However, the capacity fades continuously during cycling due to the formation of thick solid electrolyte interphase (SEI) on the surface of the electrode and the loss of active material [6].

In the present study, we report the remarkable electrochemical properties obtained for the reversible insertion of Li ions in $Al_2O_3/MoS_2/Al_2O_3$-decorated TNT layers. The capacity fading is strongly attenuated by protecting the MoS_2 nanosheets with Al_2O_3 sandwich coating, produced before and also after the MoS_2 ALD process. The 3D multilayers deliver excellent areal capacities with good stability up to 200 cycles even at very fast kinetics, making the $Al_2O_3/MoS_2/Al_2O_3$-decorated TNT layers a potential candidate as a negative electrode for high performance μLIBs.

2. Materials and Methods

2.1. Synthesis of TNTs and ALD-Decorated TNTs

Self-organized TNT layers with a thickness of ~20 μm and an inner diameter of ~110 nm were produced via anodization of thin Ti foils (127 μm thick, Sigma-Aldrich) according to the previous published work [39]. In brief, the Ti foils were anodized in an ethylene glycol-based electrolyte containing NH_4F (170 mM) and 1.5 vol % H_2O at 60 V for 4 h. Prior to anodization the Ti foils were degreased by sonication in isopropanol and acetone for 60 s, respectively, and dried in air. The anodization setup consisted of a high-voltage potentiostat (PGU-200 V; Elektroniklabor GmbH) in a two-electrode configuration, with a Pt foil as a counter electrode and the Ti foil as a working electrode. After anodization, the TNT layers were sonicated in isopropanol for 5 min and dried in air. Before further use, the TNT layers were annealed in air in a muffle oven at 400 °C for 1 h to obtain crystalline anatase phase.

The samples were coated using atomic layer deposition (ALD) (Beneq TFS-200) with 15 cycles MoS_2 (henceforth named as MoS_2-TNTs) or with a three-layer coating consisting of 9 cycles Al_2O_3—15 cycles MoS_2—9 cycles Al_2O_3 (henceforth referred as $Al_2O_3/MoS_2/Al_2O_3$-TNTs). The coating of MoS_2 was carried out as described in our previous work with bis(t-butylimido)bis(dimethylamino) molybdenum (Strem, 98%) and hydrogen sulfide (99.5%) as molybdenum and sulphur precursors, respectively [6]. The MoS_2 was deposited within the TNT layers by applying 15 ALD cycles at a temperature of 275 °C with N_2 (99.9999%) as carrier gas at a flow rate of 500 standard cubic centimeters per min (sccm). The molybdenum precursor was heated up to 75 °C to increase its vapor pressure. Under these deposition conditions, one growth ALD cycle was defined by the following sequence: Bis(t-butylimido)bis(dimethylamino) molybdenum pulse (4 s)—Bis(t-butylimido)bis (dimethylamino) molybdenum exposure (45 s)—N_2 purge (90 s)—H_2S pulse (2.5 s)—H_2S exposure (45 s)—N_2 purge (90 s).

The coating of Al_2O_3 on the TNT layers was prepared using trimethylaluminum (TMA, Strem, 99.999+%) and deionized water (18 MΩ) as aluminum and oxygen precursors, respectively [29,39]. Under these conditions, one ALD Al_2O_3 growth cycle was defined by the following sequence:

TMA pulse (500 ms)—TMA exposure (5 s)—N_2 purge (10 s)—H_2O pulse (500 ms)—H_2O exposure (5s)—N_2 purge (10 s). All processes were carried out at a temperature of 150 °C, using N_2 (99.9999%) as the carrier gas, at a flow rate of 400 sccm. The ALD process of 9 cycles Al_2O_3 corresponds to a nominal thickness of 1 nm Al_2O_3, as shown in our previous work [29].

2.2. Materials Characterization

The morphology and chemical composition of the fresh and cycled electrodes were characterized by a field emission electron microscope (FE-SEM JEOL JSM 7500F, JEOL, Tokyo, Japan) and a transmission electron microscope (Titan Themis 60–300, Thermo Fisher Scientific, Eindhoven, Netherlands) operated at 300 keV and equipped with a high angle annular dark field detector for scanning transmission electron microscopy (STEM-HAADF) and Super-X energy dispersive X-ray (EDX) spectrometer with 4×30 mm^2 windowless silicon drift detectors. All the EDX elemental maps are shown in net intensities, which represent the count intensities according to the background corrected and fitted model performed by Velox 2.9 software. Cross section views were obtained from mechanical bended TNTs. Dimensions of the layers were measured and statistically evaluated using proprietary Nanomeasure software.

The surface chemical state of MoS_2 was monitored by X-ray photoelectron spectroscopy (XPS) (ESCA2SR, Scienta-Omicron, Taunusstein, Germany) using a monochromatic Al Kα (1486.7 eV) X-ray source operated with 250W and 12.5kV. The binding energy scale was referenced to adventitious carbon (284.8 eV).

2.3. Electrochemical Characterization

The electrochemical performance tests were performed using standard two-electrode Swagelok cells that were assembled in a glovebox filled with high purity argon (Ar). The half-cells consist of as-prepared TNTs, MoS_2-TNTs, or $Al_2O_3/MoS_2/Al_2O_3$-TNTs as the working electrode and Li foil (1 mm in thickness and 9 mm in diameter) as the reference electrode. The two electrodes were separated by a Whatman glass microfiber soaked in organic liquid electrolyte solution (0.35 mL) composed of 1M $LiPF_6$ dissolved in a 1:1 vol.% mixture of ethylene carbonate (EC) and dimethyl carbonate (DMC).

The electrochemical performance tests (cyclic voltammetry, CV, galvanostatic charge−discharge) were performed using a VMP3 potentiostat (Bio Logic, France). The CV curves were recorded in a potential window of 0.01–3 V at a scan rate of 1 mV s^{-1}. Galvanostatic tests were performed at multiple C-rate in the potential window of 0.01–3 V. The current was applied based on TNTs assuming a porosity of 70.5%. The porosity calculation is based on the amount of the TNTs per cm^2 and should be noted that it is only an estimated value (see supplementary materials for the calculations). C/n means the battery is fully charged or discharged up to its total storage capacity in n hours (for this work 1C = 340 μA cm^{-2}). As the surface area of the as-prepared and ALD-decorated TNTs are macroscopic (0.82 cm^2), the obtained capacities are given in areal capacities (mAh cm^{-2}).

3. Results and Discussion

The highly ordered TNT layers were 20 μm thick, and the nanotubes had an inner diameter of ~110 nm resulting in an aspect ratio of 180, as shown in our previous publication [6]. As the amount of MoS_2 decorated on the TNT layers by 15 ALD cycles is very low, it was not possible to visualize it by using SEM. However, as proved previously by STEM-EDX, already 2 ALD cycles of MoS_2 led to a decoration of the TNT layers with small MoS_2 sheets [6].

Figure 1 shows a STEM-HAADF image of the edge of TNT decorated with 9 cycles Al_2O_3—15 cycles MoS_2—9 cycles Al_2O_3 and the corresponding EDX maps (see Figure S1a for the EDX spectrum). These maps reveal a homogenous distribution of Mo and S as well as of Al on the TNT wall. In comparison with our previous publication, the MoS_2 nanosheets appear smaller [6]. This can be explained by the different chemical nature of the surfaces that MoS_2 was deposited on: herein, the MoS_2 was deposited on the Al_2O_3 layer, while in our previous publication the MoS_2 was deposited directly

on the TNT walls [6]. The initial ALD growth of MoS_2 is different on different surfaces, and, thus, MoS_2 nanosheets observed herein are smaller than if they are directly grown on TiO_2.

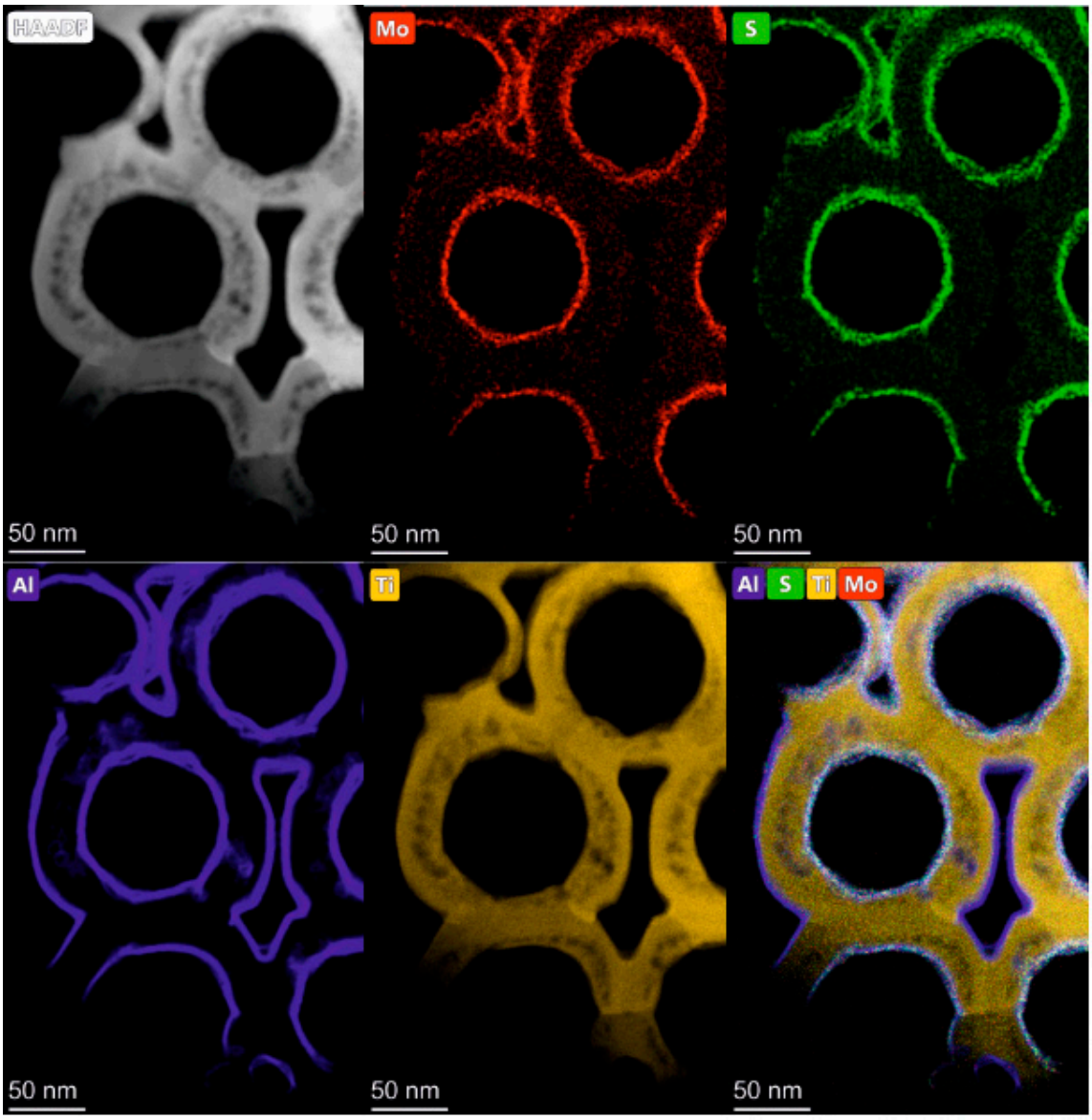

Figure 1. STEM-HAADF image in high magnification and the STEM EDX elemental maps showing the distribution of Mo, S, and Al on the surface of the TiO_2 nanotube layers (TNTs).

XPS survey spectra of TNT layers decorated with 15 cycles MoS_2 and with 9 cycles Al_2O_3—15 cycles MoS_2—9 cycles Al_2O_3 are shown in Figure 2a. For 15 cycles MoS_2 sample, Ti 2p and O 1s signals stem from the underlying TNT layer. In the case of the sandwich sample it is observed that the intensity of the O 1s signal increases and the Ti 2p decreases, due to the presence of the Al_2O_3 layers; therefore most of the O 1s comes from the Al_2O_3. The C species detected on both TNT layers are related to adventitious carbon. Figure 2b shows the corresponding Mo 3d high-resolution spectra (HR) along with the S 2s signal. As can be seen, the HR signals on both samples are relatively broad. This can be explained by the very thin MoS_2 decoration as on the TiO_2/MoS_2 interface, as well as on the Al_2O_3/MoS_2 some Mo-O bonds might be built. When higher ALD MoS_2 cycle numbers were applied (results not shown), the signals became narrower due to thicker MoS_2 nanosheet decorations, and the XPS spectra showed pure MoS_2 [6]. Considering this, Mo 3d HR spectra of both samples show their corresponding spin–orbit Mo $3d_{5/2}$/Mo $3d_{3/2}$ and were deconvoluted into three doublets. The first one (red), centered

at ~229.0/232.1 eV, is assigned to Mo^{4+} belonging to the MoS_2 lattice [40,41]. The second one (blue), located at ~229.9/233.0 eV, is attributed to Mo bonded with oxygen to form MoO_2 [42]. The last doublet (orange) at ~232.5/235.6 eV corresponds to MoO_3 [43,44]. It is notable that in the sandwich sample the signals corresponding to MoS_2 decrease, while molybdenum oxide signals increase. This could be due to the interaction of MoS_2 with the water used as a precursor for the synthesis of Al_2O_3. Besides, S 2s peaks of the 15 cycles MoS_2 sample, centered at ~226.6 (MoS_2) (dark cyan) and 229.5 eV (SH—thiol groups) (purple), respectively, and S 2s peaks of the sandwich sample, located at 226.8 (MoS_2) (dark cyan) and 234.2 (SO_4^{2-}) (green), respectively, agree well with the chemical species observed in S 2p. In Figure 2c, the deconvoluted HR S 2p spectra of both samples confirm the presence of MoS_2 with the doublet $S2p_{3/2}/S2p_{1/2}$ (dark cyan), centered at ~161.9/163.1 eV, which corresponds to the S^{2-} state from the MoS_2 lattice [45]. However, each sample presented two different additional chemical species. 15 cycles MoS_2 sample show another doublet (purple) at ~163.6/164.8 eV attributed to SH that remained on the surface after the MoS_2 deposition [46]. The sandwich sample displayed its doublet (green) at ~167.8/169.0 eV, assigned to SO_4^{2-} (sulfate) [46], possibly due to the interaction of sulfur with the water used in Al_2O_3 synthesis.

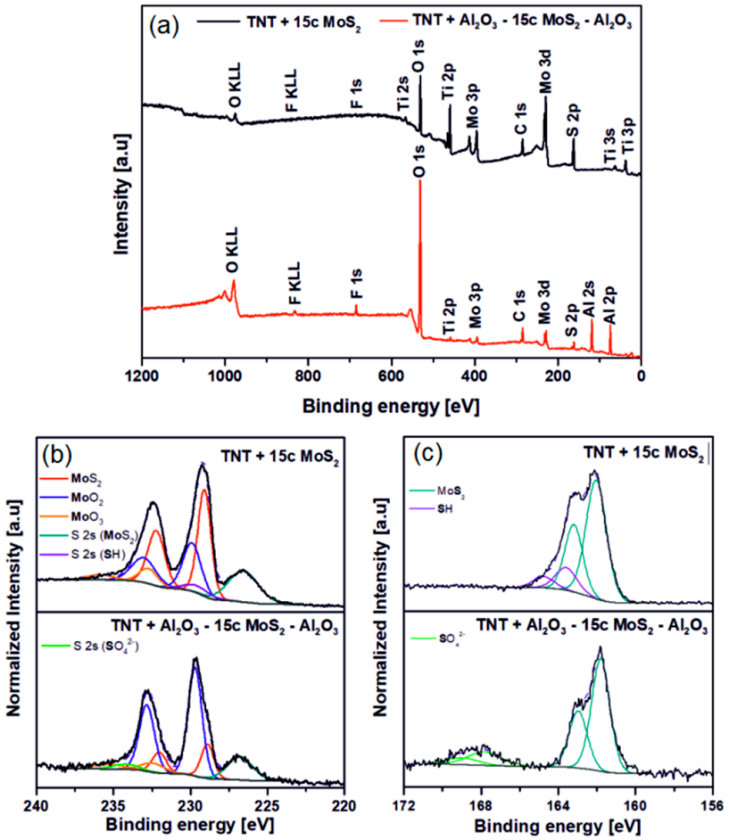

Figure 2. (**a**) X-ray photoelectron spectroscopy (XPS) survey spectra, (**b**) Mo 3d high resolution spectra and (**c**) S 2p high resolution spectra for TNT layers decorated with 15 cycles MoS_2 and with 9 cycles Al_2O_3—15 cycles MoS_2—9 cycles Al_2O_3.

Figure 3a–c shows the cyclic voltammetry curves obtained for as-prepared TNTs, MoS_2-TNTs and $Al_2O_3/MoS_2/Al_2O_3$-TNTs recorded at a scan rate of 1 mV s^{-1} in the potential window of 0.01–3 V vs. Li/Li^+. All the CV curves obtained exhibit a cathodic peak at 1.7 V vs. Li/Li^+ and anodic peak at 2.2 V vs. Li/Li^+ associated to the reversible insertion/extraction of Li^+ into/from anatase according to Equation (1) [5,18,47,48]. However, the first insertion peak for $Al_2O_3/MoS_2/Al_2O_3$-TNTs is shallow and shifts to the lower potential because of the Al_2O_3 insulating coating which slows down

the Li-diffusion [29]. This behavior is not observed in the subsequent cycles due to the formation of a conductive Al-O-Li phase.

$$TiO_2 + xLi^+ + xe^- \rightleftharpoons Li_xTiO_2 \quad 0 \le x \le 1, \tag{1}$$

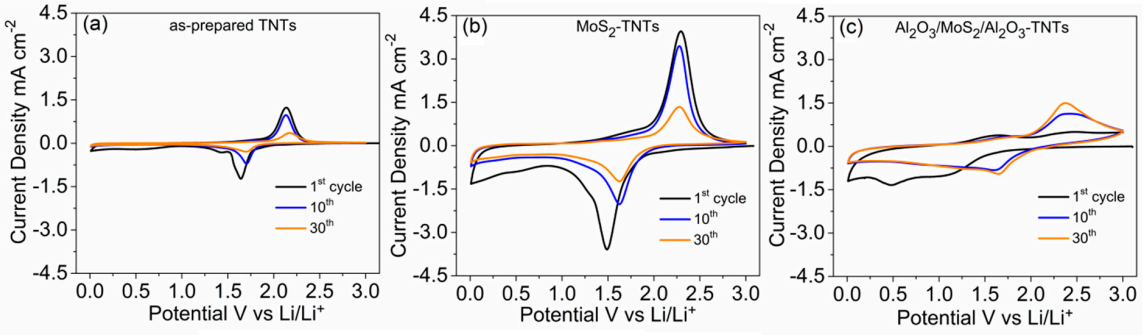

Figure 3. Cyclic voltammograms of (**a**) as-prepared TNTs, (**b**) MoS_2-TNTs and (**c**) $Al_2O_3/MoS_2/Al_2O_3$-TNTs recorded at a scan rate of 1 mV s^{-1}

In comparison to as-prepared TNTs, the CV curves show additional peaks for the MoS_2-TNTs (Figure 3b) and $Al_2O_3/MoS_2/Al_2O_3$-TNTs (Figure 3c). These peaks are attributed to the multistep reaction of Li^+ with MoS_2. During the first discharge (lithiation), the two cathodic peaks at 1.25–1.75 V and 0.5 V vs. Li/Li^+ are attributed to phase transformation of MoS_2 in to Li_xMoS_2 and the subsequent complete reduction of Mo^{4+} to Mo^0 and Li_2S, respectively, according to Equations (2) and (3) [49,50]. Upon the charge (delithiation) process, the shallow peak at 1.9 vs. Li/Li^+ associated with retrieval of Li_xMoS_2 from Mo is dwarfed by the broader and more prominent peak at 2–2.75 V *vs.* Li/Li^+, which correspond to the oxidation of Li_2S to S according to Equations (3) and (4), respectively [49,50]. This phenomenon is more pronounced for MoS_2-TNTs because of the absence of the protective Al_2O_3-coating layer.

$$MoS_2 + xLi^+ + xe^- \rightarrow Li_xMoS_2, \tag{2}$$

$$Li_xMoS_2 + (4 - x)\ Li^+ + (4 - x)\ e^- \rightleftharpoons Mo + 2Li_2S, \tag{3}$$

$$Li_2S \rightleftharpoons 2Li^+ + S + 2e^-, \tag{4}$$

Compared to the CV curves of as-prepared TNTs and $Al_2O_3/MoS_2/Al_2O_3$-TNTs, the MoS_2-TNTs shows broader peaks and larger surface area under the CV curve. This is attributed to the MoS_2-decoration contributing to the total capacity and modification of the electrode structure. However, the peak intensity and area under the CV curve diminish with cycling. In our previous work, we reported that electrochemical performance of MoS_2-TNTs is affected by the dissolution of S combined to the formation and growth of a SEI layer [6]. In contrast, reversible and stable CV curves are obtained for $Al_2O_3/MoS_2/Al_2O_3$-TNTs owing to the ALD-deposited Al_2O_3 thin layers. The surface modification results in the improved stability of the electrode by limiting the S dissolution and the growth of the SEI layer through the formation of a stable Al-O-Li composite [29].

The electrochemical performance was evaluated through the examination of the charge/discharge profiles obtained by galvanostatic cycling tests. Figure 4a–c, shows the galvanostatic charge/discharge profiles for as-prepared TNTs, MoS_2-TNTs, and $Al_2O_3/MoS_2/Al_2O_3$-TNTs at a current density of 340 μA cm^{-2} (1C) in the potential window of 0.01–3 V vs. Li/Li^+. The charge/discharge profiles are in agreement with the electrochemical behaviors observed from the CV plots. For as-prepared TNTs and MoS_2-TNTs, the obtained capacity fades with cycle number unlike to the $Al_2O_3/MoS_2/Al_2O_3$-TNTs. This is attributed to the beneficial effects of the Al_2O_3-coating on the TNTs, which are in agreement with works reported in the literature [25,29,51,52].

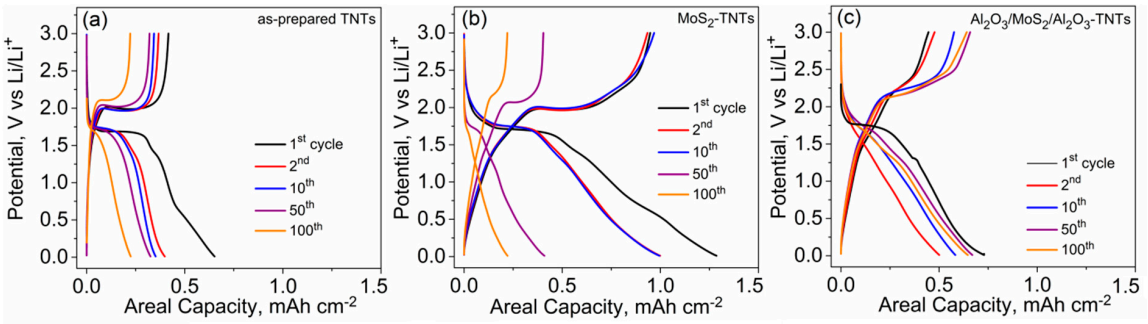

Figure 4. Galvanostatic charge/discharge profiles of (**a**) as-prepared TNTs, (**b**) MoS_2-TNTs, and (**c**) $Al_2O_3/MoS_2/Al_2O_3$-TNTs at 1C.

Figure 5a shows the discharge capacity vs. cycle number for as-prepared TNTs, MoS_2-TNTs, and $Al_2O_3/MoS_2/Al_2O_3$-TNTs cycled at 1C. The first cycle delivers a discharge capacity of 652 μAh cm^{-2}, 1286 μAh cm^{-2}, and 729 μAh cm^{-2} for the as-prepared TNTs, MoS_2-TNTs, and $Al_2O_3/MoS_2/Al_2O_3$-TNTs, respectively. The higher capacity obtained for the decorated-TNT electrodes are attributed to the contribution of MoS_2 coating. The irreversible capacity observed after the first cycle is attributed to the side reactions of Li^+ with water molecule traces and the structural defects of the TNTs, and additionally, the dissolution of S and the formation of the SEI layer in the case of MoS_2-TNTs [6,53,54]. It is clearly apparent that the $Al_2O_3/MoS_2/Al_2O_3$-TNTs have superior cyclability than as-prepared TNTs and MoS_2-TNTs with a reversible capacity of 640 μAh cm^{-2} obtained, whereas only 222 μAh cm^{-2} and 220 μAh cm^{-2} was retained after 100 cycles for the as-prepared TNTs and MoS_2-TNTs, respectively. It is remarkable that the areal capacities increase with the number of cycles. This is attributed to the formation of microcracks as the result of Li^+ reaction with MoS_2, which expose additional pore channels. In addition, the presence of Al_2O_3 decoration bestows the TNT electrodes with enhanced chemical properties. Figure 5b shows the coulombic efficiency (CE) at 1C for 100 cycles. The CE obtained for $Al_2O_3/MoS_2/Al_2O_3$-TNTs at the first cycle was 62% and reached more than 99% just after three cycles. In comparison, as-prepared TNTs and MoS_2-TNTs have a first cycle CE of 64% and 74% and reaching the 98% only after 15 and 85 cycles, respectively. These values indicate relatively more stable SEI formation on the surface of the Al_2O_3-coated electrode even after long-term cycling. It is remarkable that the beneficial effect of the Al_2O_3 coating is also evidenced at very fast kinetics (3 C) over 200 cycles as shown in Figure 5c. Indeed, the $Al_2O_3/MoS_2/Al_2O_3$-TNT electrode is able to maintain a capacity of 414 μAh cm^{-2}, whereas the as-prepared TNTs and MoS_2-TNTs retain only 130 μAh cm^{-2} and 195 μAh cm^{-2}, respectively. The main electrochemical results of the as-prepared and ALD-decorated TNTs in comparison with literature are shown in Table 1.

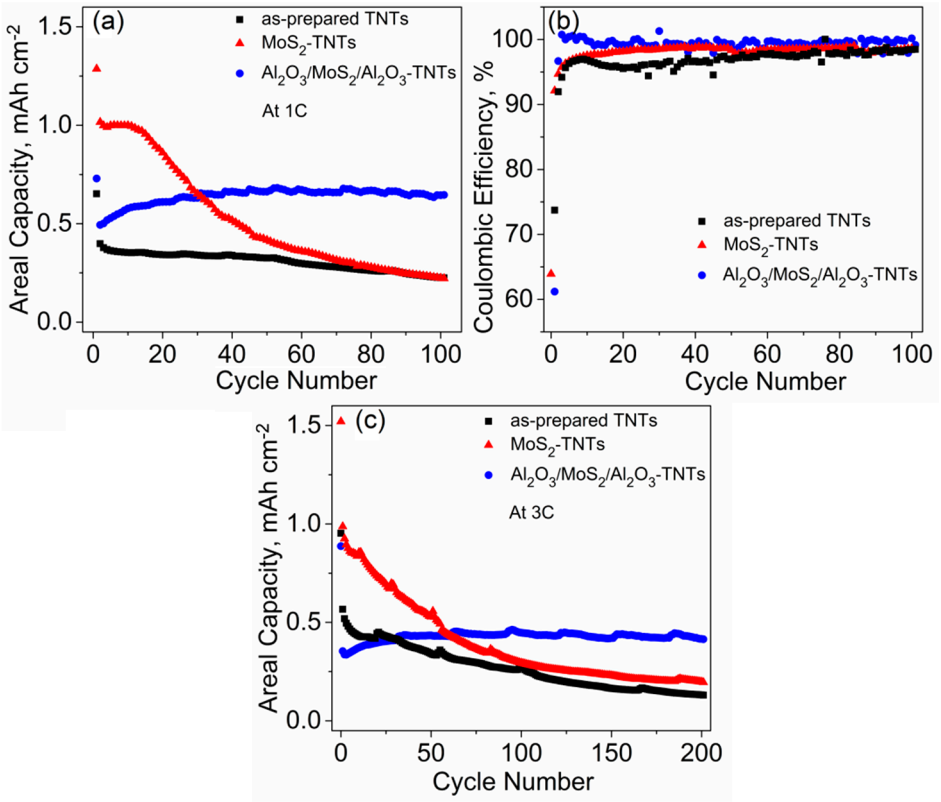

Figure 5. Long-term cycling tests of as-prepared TNTs, MoS_2-TNTs, and $Al_2O_3/MoS_2/Al_2O_3$-TNTs: (**a**) at 1C for 100 cycles, and (**b**) the corresponding coulombic efficiency vs. cycle number and (**c**) at 3C for 200 cycles.

Table 1. Comparison of the electrochemical performance of as-prepared and atomic layer deposition (ALD)-decorated TNTs with TNTs coated with various materials.

Working Electrode	First Discharge Capacity ($\mu Ah\ cm^{-2}$) at C-Rate	Discharge Capacity after (n) Cycle ($\mu Ah\ cm^{-2}$)	Coulombic Efficiency (%) after (n) Cycles
as-prepared TNTs	1C-652	222 (100)	~98% (100)
	3C-952	130 (200)	~98% (200)
MoS_2-TNTs	1C-1286	220 (100)	~98% (100)
	3C-1520	195 (200)	~98% (200)
$Al_2O_3/MoS_2/Al_2O_3$-TNTs	1C-729	640 (100)	>99% (100)
	3C-887	414 (200)	>99% (200)
SnO_2@TNTs [55]	2C-469.8	113 (50)	>94%(50)
Co_3O_4@TNTs [56]	1C-200	103 (25)	NA
TNTs@Fe_2O_3 [57]	100 mA cm^{-2}-570	680 (50)	100% (50)

Post-mortem analysis was carried out to provide further evidence for the positive contribution of the Al_2O_3 decoration on the electrochemical properties. Figure 6a–c shows the SEM images of the as-prepared TNTs, MoS_2-TNTs, and $Al_2O_3/MoS_2/Al_2O_3$-TNTs after 200 charge/discharge cycles at 3C, respectively. A very thick (ca. 6 µm) and rough SEI layer has been grown on MoS_2-TNTs (Figure 6b) in comparison to as-prepared TNTs that is around 2 µm thick (Figure 6a). Similar behavior was observed from our previous work on MoS_2-coated TNTs [6]. In contrary, the SEI formed on $Al_2O_3/MoS_2/Al_2O_3$-TNTs is much thinner (ca. 1 µm) and smoother (Figure 6c) confirming the benefit of Al_2O_3 coatings. This effect is further evidenced by STEM-EDX elemental maps given in Figure 6d showing the homogenous distribution of Mo, S, and Al on the TNT walls after electrochemical tests (see Figure S1b for the EDX spectrum).

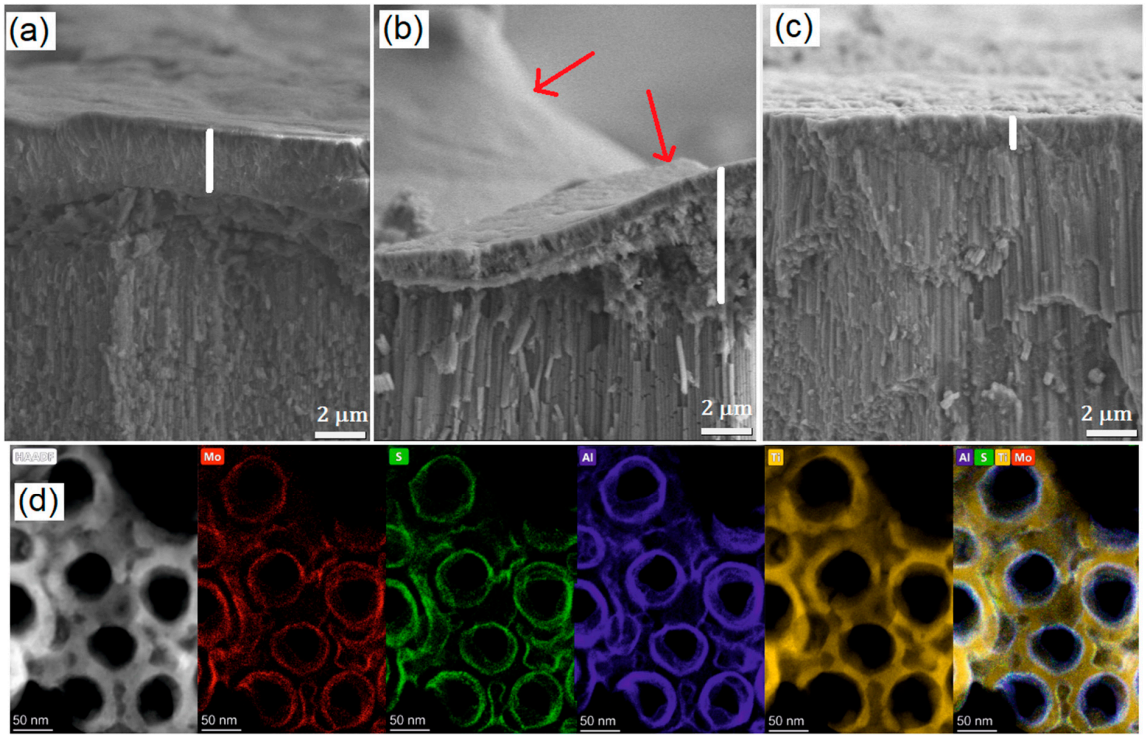

Figure 6. Cross sectional SEM images of (**a**) as-prepared TNTs, (**b**) MoS_2-TNTs, and (**c**) $Al_2O_3/MoS_2/Al_2O_3$-TNTs after 200 cycles at 3C. Solid electrolyte interphase (SEI) layer thickness and surface roughness is indicated by a white line and red arrows. (**d**) High magnification STEM HAADF image and the STEM-EDX elemental maps showing the distribution of Mo, S, and Al on the surface of the TNT for $Al_2O_3/MoS_2/Al_2O_3$-TNTs.

4. Conclusions

In this work, enhanced electrochemical performance of TNT was achieved by decorating the surface with nanosheets of MoS_2, sandwiched between Al_2O_3 coatings. ALD technique was used to homogenously deposit the MoS_2 nanosheets and the Al_2O_3 layers on the self-supporting TNT layers. The excellent capacity and stability of $Al_2O_3/MoS_2/Al_2O_3$-decorated TNT is attributed to the mechanical and structural stability imported by Al_2O_3 decoration. The Al_2O_3 limits the formation and growth of SEI layer and loss of active material during cycling. As a result, the $Al_2O_3/MoS_2/Al_2O_3$-decorated TNT deliver an areal capacity almost three times higher than that obtained for MoS_2-decorated TNT and as-prepared TNTs after 100 cycles at 1C.

Supplementary Materials: The following are available online at http://www.mdpi.com/2079-4991/10/5/953/s1. Calculation to determine the porosity of TNTs and Figure S1: EDX spectrum of $Al_2O_3/MoS_2/Al_2O_3$-TNTs (a) before and (b) after 100 galvanostatic cycles.

Author Contributions: Conceptualization, T.D. and J.M.M.; methodology, A.T.T., H.S., A.A., R.Z., J.R.-P., J.M., L.H., S.N., Z.S., and J.P.; formal analysis, A.T.T. and H.S.; writing—original draft preparation, A.T.T. and H.S.; writing—review and editing, J.M.M. and T.D.; supervision, T.D. and J.M.M.; funding acquisition, J.M.M. and T.D. All authors have read and agreed to the published version of the manuscript.

Funding: This research was funded by the European Research Council (project 638857) and Ministry of Youth, Education and Sports of the Czech Republic (LM2015082, LQ1601, CZ.02.1.01/0.0/0.0/16_013/0001829).

Acknowledgments: CzechNanoLab project LM2018110 funded by MEYS CR is gratefully acknowledged for the financial support of the TEM measurements at CEITEC Nano Research Infrastructure.

Conflicts of Interest: The authors declare no conflict of interest.

References

1. Ferrari, S.; Loveridge, M.; Beattie, S.D.; Jahn, M.; Dashwood, R.J.; Bhagat, R. Latest advances in the manufacturing of 3D rechargeable lithium microbatteries. *J. Power Sources* **2015**, *286*, 25–46. [CrossRef]
2. Nasreldin, M.; Delattre, R.; Ramuz, M.; Lahuec, C.; Djenizian, T.; de Bougrenet de la Tocnaye, J.-L. Flexible micro-battery for powering smart contact lens. *Sensors* **2019**, *19*, 2062. [CrossRef] [PubMed]
3. Wang, Y.; Liu, B.; Li, Q.; Cartmell, S.; Ferrara, S.; Deng, Z.D.; Xiao, J. Lithium and lithium ion batteries for applications in microelectronic devices: A review. *J. Power Sources* **2015**, *286*, 330–345. [CrossRef]
4. Oudenhoven, J.F.M.; Baggetto, L.; Notten, P.H.L. All-Solid-State Lithium-Ion Microbatteries: A Review of Various Three-Dimensional Concepts. *Adv. Energy Mater.* **2011**, *1*, 10–33. [CrossRef]
5. Tesfaye, A.T.; Mashtalir, O.; Naguib, M.; Barsoum, M.W.; Gogotsi, Y.; Djenizian, T. Anodized Ti_3SiC_2 as an anode material for Li-ion microbatteries. *Acs Appl. Mater. Interfaces* **2016**, *8*, 16670–16676. [CrossRef]
6. Sopha, H.; Tesfaye, A.T.; Zazpe, R.; Michalicka, J.; Dvorak, F.; Hromadko, L.; Krbal, M.; Prikryl, J.; Djenizian, T.; Macak, J.M. ALD growth of MoS_2 nanosheets on TiO_2 nanotube supports. *FlatChem* **2019**, *17*, 100130. [CrossRef]
7. Zhang, H.; Cao, Y.; Chee, M.O.L.; Dong, P.; Ye, M.; Shen, J. Recent advances in micro-supercapacitors. *Nanoscale* **2019**, *11*, 5807–5821. [CrossRef]
8. Kundu, A.; Jang, J.H.; Gil, J.H.; Jung, C.R.; Lee, H.R.; Kim, S.H.; Ku, B.; Oh, Y.S. Micro-fuel cells—Current development and applications. *J. Power Sources* **2007**, *170*, 67–78. [CrossRef]
9. Yang, Y.; Pradel, K.C.; Jing, Q.; Wu, J.M.; Zhang, F.; Zhou, Y.; Zhang, Y.; Wang, Z.L. Thermoelectric Nanogenerators Based on Single Sb-Doped ZnO Micro/Nanobelts. *Acs Nano* **2012**, *6*, 6984–6989. [CrossRef]
10. Pikul, J.H.; Zhang, H.G.; Cho, J.; Braun, P.V.; King, W.P. High-power lithium ion microbatteries from interdigitated three-dimensional bicontinuous nanoporous electrodes. *Nat. Commun.* **2013**, *4*, 1732. [CrossRef]
11. Li, W.; Christiansen, T.L.; Li, C.; Zhou, Y.; Fei, H.; Mamakhel, A.; Iversen, B.B.; Watkins, J.J. High-power lithium-ion microbatteries from imprinted 3D electrodes of sub-10 nm $LiMn_2O_4$/Li4Ti_5O_{12} nanocrystals and a copolymer gel electrolyte. *Nano Energy* **2018**, *52*, 431–440. [CrossRef]
12. Yue, C.; Li, J.; Lin, L. Fabrication of Si-based three-dimensional microbatteries: A review. *Front. Mech. Eng.* **2017**, *12*, 459–476. [CrossRef]
13. Long, J.W.; Dunn, B.; Rolison, D.R.; White, H.S. Three-dimensional battery architectures. *Chem. Rev.* **2004**, *104*, 4463–4492. [CrossRef] [PubMed]
14. Hur, J.I.; Smith, L.C.; Dunn, B. High Areal Energy Density 3D Lithium-Ion Microbatteries. *Joule* **2018**, *2*, 1187–1201. [CrossRef]
15. Zeng, W.; Zheng, F.; Li, R.; Zhan, Y.; Li, Y.; Liu, J. Template synthesis of SnO $_2$/α-Fe $_2$ O $_3$ nanotube array for 3D lithium ion battery anode with large areal capacity. *Nanoscale* **2012**, *4*, 2760–2765. [CrossRef] [PubMed]
16. Shaijumon, M.M.; Perre, E.; Daffos, B.; Taberna, P.L.; Tarascon, J.M.; Simon, P. Nanoarchitectured 3D cathodes for Li-Ion microbatteries. *Adv. Mater.* **2010**, *22*, 4978–4981. [CrossRef] [PubMed]
17. Wei, W.; Oltean, G.; Tai, C.-W.; Edstrom, K.; Bjorefors, F.; Nyholm, L. High Energy and Power Density TiO_2 Nanotube Electrodes for 3D Li-ion Microbatteries. *J. Mater. Chem. A* **2013**, *1*, 8160–8169. [CrossRef]
18. Ellis, B.L.; Knauth, P.; Djenizian, T. Three-Dimensional Self-Supported Metal Oxides for Advanced Energy Storage. *Adv. Mater.* **2014**, *26*, 3368–3397. [CrossRef]
19. Su, X.; Wu, Q.; Zhan, X.; Wu, J.; Wei, S.; Guo, Z. Advanced titania nanostructures and composites for lithium ion battery. *J. Mater. Sci.* **2012**, *47*, 2519–2534. [CrossRef]
20. Chen, Z.; Belharouak, I.; Sun, Y.K.; Amine, K. Titanium-based anode materials for safe lithium-ion batteries. *Adv. Funct. Mater.* **2013**, *23*, 959–969. [CrossRef]
21. Ortiz, G.F.; Hanzu, I.; Djenizian, T.; Lavela, P.; Tirado, J.L.; Knauth, P. Alternative Li-ion battery electrode based on self-organized titania nanotubes. *Chem. Mater.* **2009**, *21*, 63–67. [CrossRef]
22. Vacandio, F.; Fraoucene, H.; Sugiawati, V.A.; Eyraud, M.; Hatem, D.; Belkaid, M.S.; Pasquinelli, M.; Djenizian, T. Optical and Electrochemical Properties of Self-Organized TiO_2 Nanotube Arrays from Anodized Ti–6Al–4V Alloy. *Front. Chem.* **2019**, *7*, 66.
23. Myung, S.T.; Takahashi, N.; Komaba, S.; Yoon, C.S.; Sun, Y.K.; Amine, K.; Yashiro, H. Nanostructured TiO_2 and Its Application in Lithium-Ion Storage. *Adv. Funct. Mater.* **2011**, *21*, 3231–3241. [CrossRef]

24. Borghols, W.; Lützenkirchen-Hecht, D.; Haake, U.; Van Eck, E.; Mulder, F.; Wagemaker, M. The electronic structure and ionic diffusion of nanoscale LiTiO $_2$ anatase. *Phys. Chem. Chem. Phys.* **2009**, *11*, 5742–5748. [CrossRef] [PubMed]
25. Dvorak, F.; Zazpe, R.; Krbal, M.; Sopha, H.; Prikryl, J.; Ng, S.; Hromadko, L.; Bures, F.; Macak, J.M. One-dimensional anodic TiO_2 nanotubes coated by atomic layer deposition: Towards advanced applications. *Appl. Mater. Today* **2019**, *14*, 1–20. [CrossRef]
26. Salian, G.D.; Krbal, M.; Sopha, H.; Lebouin, C.; Coulet, M.-V.; Michalicka, J.; Hromadko, L.; Tesfaye, A.T.; Macak, J.M.; Djenizian, T. Self-supported sulphurized TiO_2 nanotube layers as positive electrodes for lithium microbatteries. *Appl. Mater. Today* **2019**, *16*, 257–264. [CrossRef]
27. Lu, Z.; Yip, C.T.; Wang, L.; Huang, H.; Zhou, L. Hydrogenated TiO_2 nanotube arrays as high-rate anodes for lithium-ion microbatteries. *ChemPlusChem* **2012**, *77*, 991–1000. [CrossRef]
28. Salian, G.D.; Koo, B.M.; Lefevre, C.; Cottineau, T.; Lebouin, C.; Tesfaye, A.T.; Knauth, P.; Keller, V.; Djenizian, T. Niobium Alloying of Self-Organized TiO_2 Nanotubes as an Anode for Lithium-Ion Microbatteries. *Adv. Mater. Technol.* **2018**, *3*, 1700274. [CrossRef]
29. Sopha, H.; Salian, G.D.; Zazpe, R.; Prikryl, J.; Hromadko, L.; Djenizian, T.; Macak, J.M. ALD Al2O3-Coated TiO_2 Nanotube Layers as Anodes for Lithium-Ion Batteries. *Acs Omega* **2017**, *2*, 2749–2756. [CrossRef]
30. Kyerematen, N.A.; Vacandio, F.; Sougrati, M.-T.; Martinez, H.; Jumas, J.-C.; Knauth, P.; Djenizian, T. Effect of Sn-doping on the electrochemical behaviour of TiO_2 nanotubes as potential negative electrode materials for 3D Li-ion micro batteries. *J. Power Sources* **2013**, *224*, 269–277. [CrossRef]
31. Zhu, Q.; Hu, H.; Li, G.; Zhu, C.; Yu, Y. TiO_2 nanotube arrays grafted with MnO_2 nanosheets as high-performance anode for lithium ion battery. *Electrochim. Acta* **2015**, *156*, 252–260. [CrossRef]
32. Gao, L.; Hu, H.; Li, G.; Zhu, Q.; Yu, Y. Hierarchical 3D TiO_2@ Fe_2O_3 nanoframework arrays as high-performance anode materials. *Nanoscale* **2014**, *6*, 6463–6467. [CrossRef] [PubMed]
33. Brumbarov, J.; Kunze-Liebhäuser, J. Silicon on conductive self-organized TiO_2 nanotubes–A high capacity anode material for Li-ion batteries. *J. Power Sources* **2014**, *258*, 129–133. [CrossRef]
34. Madian, M.; Giebeler, L.; Klose, M.; Jaumann, T.; Uhlemann, M.; Gebert, A.; Oswald, S.; Ismail, N.; Eychmüller, A.; Eckert, J. Self-Organized TiO_2/CoO Nanotubes as Potential Anode Materials for Lithium Ion Batteries. *Acs Sustain. Chem. Eng.* **2015**, *3*, 909–919. [CrossRef]
35. Yiping, T.; Xiaoxu, T.; Guangya, H.; Guoqu, Z. Nanocrystalline $Li4Ti_5O_{12}$-coated TiO_2 nanotube arrays as three-dimensional anode for lithium-ion batteries. *Electrochim. Acta* **2014**, *117*, 172–178. [CrossRef]
36. Sugiawati, V.A.; Vacandio, F.; Galeyeva, A.; Kurbatov, A.P.; Djenizian, T. Enhanced Electrochemical Performance of Electropolymerized Self-Organized TiO_2 Nanotubes Fabricated by Anodization of Ti Grid. *Front. Phys.* **2019**, *7*, 179. [CrossRef]
37. Plylahan, N.; Kyerematen, N.A.; Eyraud, M.; Dumur, F.; Martinez, H.; Santinacci, L.; Knauth, P.; Djenizian, T. Highly conformal electrodeposition of copolymer electrolytes into titania nanotubes for 3D Li-ion batteries. *Nanoscale Res. Lett.* **2012**, *7*, 349. [CrossRef]
38. Kyerematen, N.A.; Dumur, F.; Knauth, P.; Pecquenard, B.; Djenizian, T. Electrodeposited copolymer electrolyte into nanostructured titania electrodes for 3D Li-ion microbatteries. *C. R. Chim.* **2013**, *16*, 80–88. [CrossRef]
39. Zazpe, R.; Knaut, M.; Sopha, H.; Hromadko, L.; Albert, M.; Prikryl, J.; Gartnerova, V.; Bartha, J.W.; Macak, J.M. Atomic layer deposition for coating of high aspect ratio TiO_2 nanotube layers. *Langmuir* **2016**, *32*, 10551–10558. [CrossRef]
40. Stevens, G.; Edmonds, T. Catalytic activity of the basal and edge planes of molybdenum disulphide. *J. Less Common Met* **1977**, *54*, 321–330. [CrossRef]
41. Ganta, D.; Sinha, S.; Haasch, R.T. 2-D material molybdenum disulfide analyzed by XPS. *Surf. Sci. Spectra* **2014**, *21*, 19–27. [CrossRef]
42. Benoist, L.; Gonbeau, D.; Pfister-Guillouzo, G.; Schmidt, E.; Meunier, G.; Levasseur, A. XPS analysis of lithium intercalation in thin films of molybdenum oxysulphides. *Surf Interface Anal* **1994**, *22*, 206–210. [CrossRef]
43. Hopfengärtner, G.; Borgmann, D.; Rademacher, I.; Wedler, G.; Hums, E.; Spitznagel, G. XPS studies of oxidic model catalysts: Internal standards and oxidation numbers. *J Electron Spectros Relat Phenom.* **1993**, *63*, 91–116. [CrossRef]
44. Patterson, T.A.; Carver, J.C.; Leyden, D.E.; Hercules, D.M. A surface study of cobalt-molybdena-alumina catalysts using x-ray photoelectron spectroscopy. *J. Phys. Chem.* **1976**, *80*, 1700–1708. [CrossRef]

45. Alstrup, I.; Chorkendorff, I.; Candia, R.; Clausen, B.S.; Topsøe, H. A combined X-Ray photoelectron and Mössbauer emission spectroscopy study of the state of cobalt in sulfided, supported, and unsupported Co Mo catalysts. *J. Catal.* **1982**, *77*, 397–409. [CrossRef]
46. Moulder, J.F.; Stickle, W.F.; Sobol, P.E.; Bomben, K.D. *Handbook of X-ray Photoelectron Spectroscopy: A Reference Book of Standard Spectra for Identification and Interpretation of XPS Data*, Perkin Elmer Corp., Physical Electronics Division: EdenPrairie, MN, USA, 1995.
47. Van de Krol, R.; Goossens, A.; Schoonman, J. Spatial extent of lithium intercalation in anatase TiO_2. *J. Phys. Chem. B* **1999**, *103*, 7151–7159. [CrossRef]
48. Tesfaye, A.T.; Gogotsi, Y.; Djenizian, T. Tailoring the morphological properties of anodized Ti_3 SiC_2 for better power density of Li-ion microbatteries. *Electrochem. Commun.* **2017**, *81*, 29–33. [CrossRef]
49. Wu, C.-Y.; Chang, W.-E.; Sun, Y.-G.; Wu, J.-M.; Duh, J.-G. Three-dimensional S-MoS_2@α-Fe_2O_3 nanoparticles composites as lithium-ion battery anodes for enhanced electrochemical performance. *Mater. Chem. Phys.* **2018**, *219*, 311–317. [CrossRef]
50. Wang, L.; Zhang, Q.; Zhu, J.; Duan, X.; Xu, Z.; Liu, Y.; Yang, H.; Lu, B. Nature of extra capacity in MoS2 electrodes: Molybdenum atoms accommodate with lithium. *Energy Storage Mater.* **2019**, *16*, 37–45. [CrossRef]
51. Balach, J.; Jaumann, T.; Giebeler, L. Nanosized Li2S-based cathodes derived from MoS_2 for high-energy density Li–S cells and Si–Li_2S full cells in carbonate-based electrolyte. *Energy Storage Mater.* **2017**, *8*, 209–216. [CrossRef]
52. Lindström, H.; Södergren, S.; Solbrand, A.; Rensmo, H.; Hjelm, J.; Hagfeldt, A.; Lindquist, S.-E. Li+ ion insertion in TiO_2 (anatase). 2. Voltammetry on nanoporous films. *J. Phys. Chem. B* **1997**, *101*, 7717–7722. [CrossRef]
53. Lipson, A.L.; Puntambekar, K.; Comstock, D.J.; Meng, X.; Geier, M.L.; Elam, J.W.; Hersam, M.C. Nanoscale investigation of solid electrolyte interphase inhibition on Li-ion battery MnO electrodes via atomic layer deposition of Al_2O_3. *Chem. Mater.* **2014**, *26*, 935–940. [CrossRef]
54. Plylahan, N.; Letiche, M.; Barr, M.K.S.; Ellis, B.; Maria, S.; Phan, T.N.; Bloch, E.; Knauth, P.; Djenizian, T. High energy and power density TiO_2 nanotube electrodes for single and complete lithium-ion batteries. *J. Power Sources* **2015**, *273*, 1182–1188. [CrossRef]
55. Wu, X.; Zhang, S.; Wang, L.; Du, Z.; Fang, H.; Ling, Y.; Huang, Z. Coaxial SnO_2@ TiO_2 nanotube hybrids: From robust assembly strategies to potential application in Li+ storage. *J. Mater. Chem.* **2012**, *22*, 11151–11158. [CrossRef]
56. Kyerematen, N.A.; Lebouin, C.; Knauth, P.; Djenizian, T. The electrochemical behaviour of TiO_2 nanotubes with Co_3O_4 or NiO submicron particles: Composite anode materials for Li-ion micro batteries. *Electrochim. Acta* **2013**, *88*, 814–820. [CrossRef]
57. Yu, L.; Wang, Z.; Zhang, L.; Wu, H.B.; Lou, X.W.D. TiO_2 nanotube arrays grafted with Fe_2O_3 hollow nanorods as integrated electrodes for lithium-ion batteries. *J. Mater. Chem. A* **2013**, *1*, 122–127. [CrossRef]